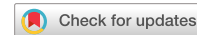


# communications materials

ARTICLE



<https://doi.org/10.1038/s43246-021-00210-6>

OPEN

## Utilizing local phase transformation strengthening for nickel-base superalloys

Timothy M. Smith<sup>1</sup>✉, Nikolai A. Zarkevich<sup>2</sup>, Ashton J. Egan<sup>3</sup>, Joshua Stuckner<sup>1</sup>, Timothy P. Gabb<sup>1</sup>, John W. Lawson<sup>2</sup> & Michael J. Mills<sup>3</sup>

Almost 75 years of research has been devoted to producing superalloys capable of higher operating temperatures in jet turbine engines, and there is an ongoing need to increase operating temperature further. Here, a new disk Nickel-base superalloy is designed to take advantage of strengthening atomic-scale dynamic complexions. This local phase transformation strengthening provides the alloy with a three times improvement in creep strength over similar disk superalloys and comparable strength to a single crystal blade alloy at 760 °C. Ultra-high-resolution chemical mapping reveals that the improvement in creep strength is a result of atomic-scale  $\eta$  ( $D0_{24}$ ) and  $\chi$  ( $D0_{19}$ ) formation along superlattice stacking faults. To understand these results, the energy differences between the  $L1_2$  and competing  $D0_{24}$  and  $D0_{19}$  stacking fault structures and their dependence on composition are computed by density functional theory. This study can help guide researchers to further optimize local phase transformation strengthening mechanisms for alloy development.

<sup>1</sup> NASA Glenn Research Center, 21000 Brook Park Rd., Cleveland, OH 44135, USA. <sup>2</sup> Intelligent Systems Division, NASA Ames Research Center, 258 Allen Rd., Moffett Field, CA 94035, USA. <sup>3</sup> Department of Materials Science and Engineering, The Ohio State University, 140 W 19th Ave., Columbus, OH 43210, USA. ✉email: [timothy.m.smith@nasa.gov](mailto:timothy.m.smith@nasa.gov)

Nickel-based superalloys are primarily designed for critical high-temperature energy and aerospace applications such as in jet engine turbine disks<sup>1</sup>. Throughout the last century, this alloy system has been incrementally improved through alloying, by incorporating the strengthening Ni<sub>3</sub>Al γ' precipitates<sup>2</sup>, grain boundary strengtheners (C, B)<sup>3</sup>, and solid-solution strengtheners using refractory elements such as W, Re, Ta, Mo, etc<sup>4</sup>. These small chemical additions combined with processing improvements, such as powder metallurgy and single crystal fabrication, have helped to realize the highly efficient turbine engines being designed today. Still, this pursuit of improved high-temperature alloys is unending, as the aerospace industry aims to further increase the efficiency of future engines to reduce CO<sub>2</sub> emissions and fuel consumption.

Recent advances in high-resolution characterization techniques such as atomic resolution scanning transmission electron microscopy (STEM) and energy-dispersive x-ray spectroscopy (EDS) have coincided with an improved understanding of how atomic-scale microstructure and deformation can affect an alloy's properties<sup>5,6</sup>. One such discovery was the presence of atomic-scale phase transformations along grain boundaries in metallic alloys<sup>7,8</sup>. These features called, "complexions" have been found to affect a wide range of material properties, from reducing electrical resistivity in Cu alloys<sup>9</sup>, to improving plasticity in Mg alloys<sup>10</sup>. In these cases, the presence of complexions was a static occurrence that was created when processing the alloy and did not evolve from the material's use. However, alloys that are used in extreme environments such as Ni-based superalloys present the possibility of "dynamic complexions" that could be initiated during a jet engine's operation to actively strengthen the alloy. In fact, multiple past studies have noted the presence of dynamic complexions in creep Ni- and Co-based superalloys, where faulted regions of the strengthening γ' precipitates consisted of chemical segregation similar to the softer γ phase<sup>6,11–15</sup>. This subsequent low-energy γ-like structure along the γ' faults was found to be detrimental to the creep strength of the alloy by providing a region through the precipitate that subsequent dislocations could more easily shear thus increasing the creep strain rate of the alloy<sup>16</sup>.

Recently, the possibility arose that this softening effect could be avoided during creep by instead promoting strengthening ordered phases along stacking faults (SFs)<sup>17–19</sup>. It was discovered that a Ni-based disk alloy, ME501, containing higher amounts of Ta, Nb, and Ti formed a creep-induced ordered η phase along superlattice extrinsic stacking faults (SEFs) instead of the usually observed γ-like segregation. The occurrence of this local η phase LPT correlated with improved creep strength of ME501 relative to a γ phase LPT forming (ME3) alloy<sup>18</sup>. This finding revealed that segregation along SFs could be manipulated through subtle compositional changes that improve an alloy's creep properties and was coined local phase transformation (LPT) strengthening.

Independently, it was discovered that the ordered Co<sub>3</sub>(W, Mo) χ phase could form along superlattice intrinsic stacking faults (SISFs) in superalloys<sup>19</sup> and again appeared to improve creep properties<sup>17</sup>. Through DFT calculations and experimental observation, it was shown that the formation of an ordered χ phase along SISFs would inhibit further shearing of the fault into an anti-phase boundary (APB). By suppressing this shear process, stacking fault ribbons would become immobile when trying to shear a γ' precipitate<sup>20,21</sup>. Thus, as was the case with the previously described η phase transformation along SEFs, this χ phase transformation represented another novel LPT strengthening mechanism that could be employed to develop more creep-resistant alloys<sup>17</sup>.

So collectively, in the last few years two new dynamic strengthening techniques (η and χ) have been discovered for powder metallurgy (PM) produced Ni-based disk superalloys.

A study by Lilensten et al.<sup>22</sup> revealed that an alloy with high Nb content could promote both the η phase and χ phase and suggested other possible compositional routes could be explored that take advantage of these new dynamic strengthening techniques. The objective of the present study is to confirm the ability to improve the creep resistance of future high-temperature alloys by promoting the formation of both the η and χ phases in a new disk alloy, based on the results and compositions of alloys in past work<sup>17,18</sup>. In addition, first-principles modeling<sup>23</sup> based on density functional theory (DFT) was performed to explore relative structural stability and to point at the alloying elements that could be used to promote and optimize these dynamic LPT strengthening formations. Both experimental and theoretical findings reveal the relationship between chemistry and this novel dynamic strengthening technique.

## Results

**Heat treatment/microstructure of TSNA-1.** Powder was sealed in a container and consolidated by hot isostatic pressurization (HIP). The chemical homogeneity of the consolidated alloy was examined using a LECO CS-444-LS carbon/sulfur determinator, a LECO TC-436 N/O determinator, and a Varian Vista Pro Inductively Coupled Plasma (ICP) Emission Spectrometer for boron and the metallic elements to measure composition from the top and bottom sections of the billet. The measured chemistry for each sample is presented in supplementary Table 1 which reveals no notable difference in composition between the top and bottom sections of the TSNA-1 billet. A preliminary exploration of the HIPed microstructure in TSNA-1 revealed both primary γ' and bulk η phases which are undesirable for optimal mechanical properties<sup>24</sup>. In order to remove these detrimental phases three different one-hour solution heat treatments (1170 °C, 1180 °C, 1190 °C) were performed. EBSD orientation maps of the TSNA-1 microstructure resulting from each solution temperature are presented in supplementary Fig. 1.

A coarser grain structure was correlated with increasing solution temperatures. The average grain size almost doubled between the 1170 °C and 1180 °C solution temperatures from 8.5 μm to 16.6 μm, respectively. The 1190 °C solution temperature provided a modest increase in grain size to 19.2 μm. All three measurements are significantly below the near 60 μm grain diameters possessed by the forged and extruded ME3 and LSHR alloys which highlight the need for forging or extruding this material to achieve large grain structures<sup>25</sup>. Each TSNA-1 solution was then given the conventional two-step ageing heat treatment used for LSHR<sup>26</sup>. Supplementary Fig. 2 provides micrographs from the 1190 °C heat-treated TSNA-1 specimen as it was the only process that resulted in a bulk η-free microstructure.

Both Nb-rich carbides and Mo/W-rich borides were found present throughout the microstructure from SEM-EDS analysis. Hf-oxide inclusions were also observed. These oxides contributed to prior particle boundaries (PPB), which are both evident in supplementary Fig. 2(a) and 2(b) as arrays of inclusions. PPB are the result of surface oxides and contamination present on the alloy powder during HIP which remain after consolidation. PPB are more common in HIP material that has not been forged<sup>27</sup>. PPB are usually considered detrimental to mechanical properties such as ductility<sup>28</sup>. γ' etched micrographs of TSNA-1 are shown in Fig. 1.

Figure 1(a), 1(b) further confirms that the 1190 °C solution and two-step ageing heat treatment produced the pursued γ/γ' microstructure needed for this class of alloy. In Fig. 1(b) coarse secondary γ' precipitates can be observed with some fine tertiary γ' precipitates apparent in the γ channels. Table 1 compares the γ'

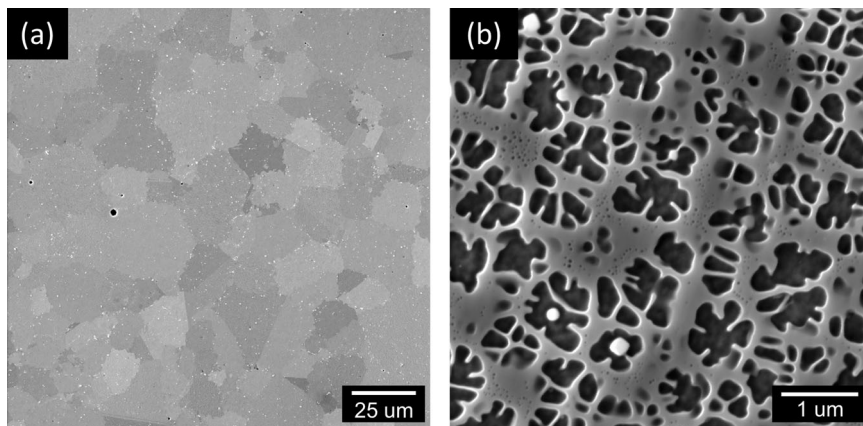


**Fig. 1 Micrographs of grain and precipitate structure in TSNA-1.** **a** SEM micrograph of TSNA-1 post heat treatment (1190 °C solution). **b** The  $\gamma/\gamma'$  microstructure from a  $\gamma'$ -etched specimen in SEM using a secondary detector after aging.

**Table 1 Precipitate Characterization.**

(c) Alloy	Secondary $\gamma'$ VF	Tertiary $\gamma'$ VF	Total $\gamma'$ VF	Average Secondary $\gamma'$ Size	Average Tertiary $\gamma'$ Size
ME3	$44.8 \pm 0.5\%$	$2.6 \pm 0.2\%$	$47.4 \pm 0.6\%$	234 nm	36.4 nm
LSHR	$45.4 \pm 1.8\%$	$3.4 \pm 0.4\%$	$48.7 \pm 1.3\%$	243 nm	39.8 nm
TSNA-1	$54.0 \pm 0.2\%$	$0.6 \pm 0.2\%$	$54.5 \pm 0.3\%$	311 nm	38.5 nm

Quantified  $\gamma'$  precipitate size and volume fraction (VF) comparison between ME3, LSHR, and TSNA-1. Errors ( $\pm$ ) represent the standard deviation.

volume fractions (VF) and average sizes for the three disk alloys. ME3 and LSHR were found to possess similar precipitate structures while TSNA-1 had a coarser secondary  $\gamma'$  size and higher volume fraction. This higher secondary volume fraction in TSNA-1 was associated with a lower tertiary  $\gamma'$  volume fraction compared to ME3 and LSHR.

**Mechanical properties.** Results of the room temperature tensile tests of coarse grain (CG) ME3 and LSHR tensile specimen and fine grain (FG) LSHR and TSNA-1 are shown in Supplementary Table 2(a). The grain size for the FG LSHR samples was  $19.8 \mu\text{m}$  which provides a more comparable grain structure to that found in TSNA-1. At room temperature, TSNA-1 possessed a slightly higher yield strength than similar fine-grain size LSHR, both of which had higher yield strengths than either coarse grain LSHR or ME3. This higher strength at room temperature for TSNA-1 may be explained by its finer grain size and higher secondary  $\gamma'$  volume fraction. Supplementary Table 2(b) reveals the tensile strengths of the FG LSHR and TSNA-1 alloys.

At  $760^\circ\text{C}$ , TSNA-1 provided a substantially higher yield strength as compared to LSHR. This higher yield strength in TSNA-1 was also associated with higher relaxed stresses at time intervals up to 100 h as compared to LSHR. While LSHR and TSNA-1 have similar room temperature properties, the larger difference in tensile strength at elevated temperatures highlights the sensitivity of these alloys under thermally activated conditions, possibly due to the difference in active segregation between LSHR and TSNA-1.

Figure 2 presents the creep curves for CG ME3, CG LSHR, FG LSHR, FG TSNA-1, and single crystal (SX) CMSX-4 at  $760^\circ\text{C}$  and 552 MPa. TSNA-1 demonstrated a significantly lower creep strain rate as compared to ME3 and LSHR, despite its much finer microstructure ( $19 \mu\text{m}$  versus  $60 \mu\text{m}$  average grain size). The influence of average grain size on creep properties in the temperature and stress regime can be observed by comparing the creep curves for the FG and CG LSHR. It is evident that possessing a finer grain structure is detrimental to creep

performance as the FG LSHR specimen reached 0.3% inelastic creep strain in 70 h compared to 109 h for the CG sample. This suggests that microstructure cannot fully explain creep strength in this regime as TSNA-1 presented a 2-3x improvement in creep strength over the larger grained disk alloys. Even more remarkable is how similar the creep properties of TSNA-1 are to that of single-crystal CMSX-4. Interestingly, the primary creep of the alloys appears to be independent of the secondary creep strain rates. For example, CMSX-4 presents the fastest primary strain rate but transitions to a much lower secondary creep strain rate before the other disk alloys. This rapid transition to a secondary creep rate in CMSX-4 is most likely a result of the larger  $\gamma'$  volume fraction and precipitate size it possesses over the disk alloys (70 vs. 50%)<sup>29</sup>. While the primary creep strain rate is associated with the formation and glide of dislocations in the channels, the secondary creep strain rate will be more influenced by the  $\gamma'$  shearing modes<sup>30</sup>. Therefore, detailed substructure characterization of the disk alloys was conducted to determine whether the activation of different LPT strengthening mechanisms could be correlated with differences in the secondary creep strain rates between the alloys, while the primary creep strain rates are similar.

## Discussion

**Stacking fault characteristics.** TSNA-1 was designed to activate the  $\eta$  phase along SESFs which should inhibit the formation of micro twins during creep. To confirm this result STEM micrographs of the active creep deformation modes in the three disk alloys ME3, LSHR, and TSNA-1 were analyzed and are shown in Fig. 3.

Overall, the three separate disk alloys exhibited similar creep deformation substructures; dislocations glide in the  $\gamma$  channels and faulting through the precipitates. As has been noted in prior studies, the faulting in ME3 and LSHR appears to be dominated by large faults that shear both the  $\gamma$  and  $\gamma'$  phases. These extended faults were usually found to be micro twins which is a significant source of creep strain in these alloys<sup>19</sup>. However, the content of

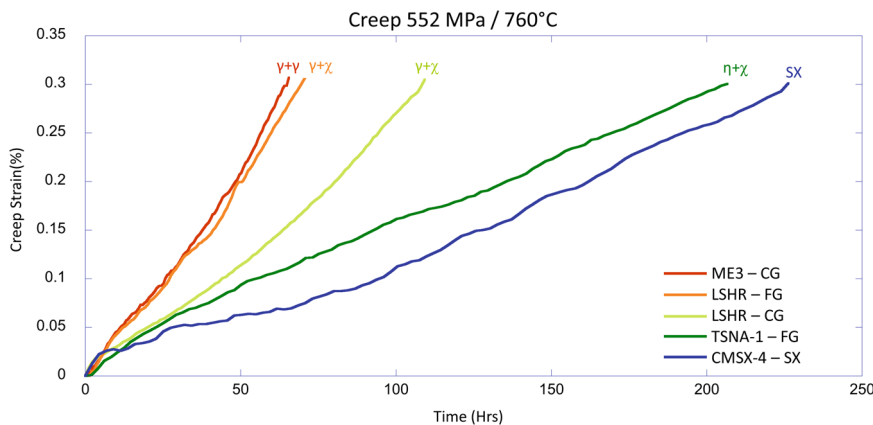


**Fig. 2 Creep curves.** Creep curves for coarse-grain ME3, coarse grain LSHR, fine grain HIP TSNA-1, and CMSX-4 at 760 °C and 552 MPa. TSNA-1 exhibited a significant improvement in creep resistance over ME3 and LSHR superalloys despite having a much finer microstructure.

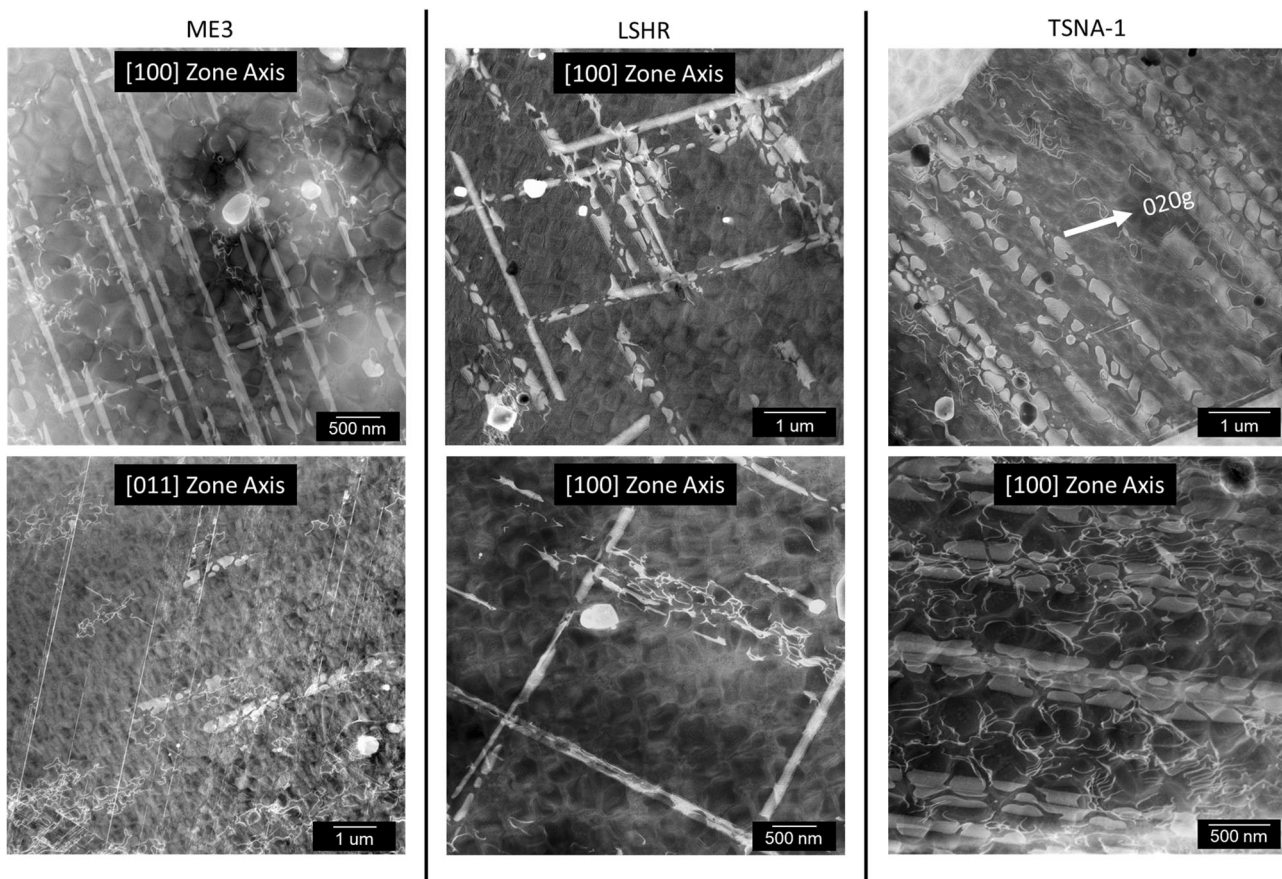


**Fig. 3 STEM micrographs of creep deformation in disk superalloys.** Representative STEM annular dark-field micrographs of active deformation structures in ME3, LSHR, and TSNA-1.

micro twins qualitatively appears to be less in the TSNA-1 alloy compared to LSHR and ME3. This observation would be consistent with past studies that have found alloys with higher amounts of Ta, Nb, and Ti suppress micro twin formation during creep by forming the ordered  $\eta$  phase along SESFs<sup>18,22</sup>.

In order to confirm that the micro twin-inhibiting  $\eta$  phase had indeed formed along SESFs in TSNA-1, atomic resolution high angle annular dark field (HAADF-STEM) [110] zone axis images and chemical maps were obtained, as shown in Fig. 4.

The HAADF-STEM zone axis micrographs of the SESF in Fig. 4(a) reveals an ordered high Z contrast along the fault<sup>31</sup>. This

familiar “grid-like” ordering present along the SESF in TSNA-1 has been previously noted in multiple alloys where the  $\eta$  phase was confirmed along the fault<sup>32</sup>. The atomic resolution chemical maps reveal that segregation of the  $\eta$  phase formers (Ti, Ta, and Nb) replace Al on its sublattice, while Co was found to replace Ni. Segregation of the  $\eta$  phase formers is presumably the main source of the increased HAADF intensity of columns at the fault. The composite map of Ni, Al, and Ta reveals how strongly the composition has been altered along the fault by the  $\gamma'$  to  $\eta$  phase transformation. The combination of both the HAADF and chemical maps confirms that a Ta and Ti-rich  $\eta$  phase has formed

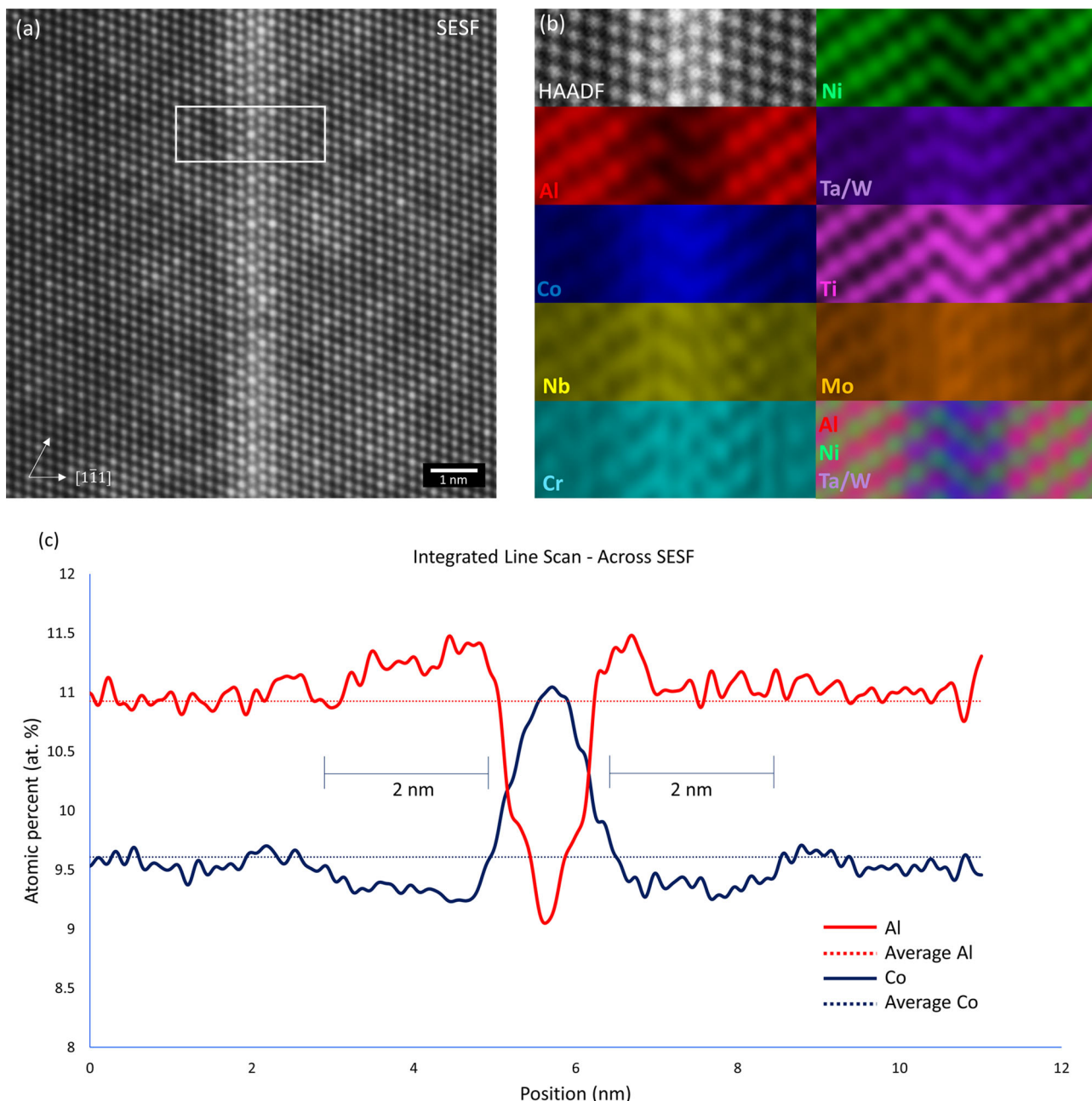


**Fig. 4 Atomic resolution characterization of a SESF in TSNA-1. **a**** HAADF STEM image of an SESF in TSNA-1 and **(b)** atomic resolution chemical maps of the SESF. The lowest right map is a composite of the Ni, Al, and Ta/W maps revealing  $\eta$  phase formation. **c** Integrated line scans of Al and Co across an SESF in TSNA-1 revealing an increase in Al content adjacent to the fault and a decrease in Co compared to the average values of the two elements.

along SESFs in TSNA-1, possibly inhibiting micro twin formation. In addition to providing remarkable, qualitative insight into the specific lattice sites an elemental species occupies along the faults, these high-resolution chemical maps also reveal compositional changes to the  $\gamma'$  precipitate adjacent to the faults. In Fig. 4(c), the integrated line scans of Al and Co across an SESF in TSNA-1 reveal that the segregation of Co along the fault is associated with a depletion of Co adjacent to it. In contrast, for Al, the depletion of Al along the fault is accompanied by an enrichment of Al in the surrounding  $\gamma'$  adjacent to the fault. The dotted lines in Fig. 4(c) represent the average Al and Co content taken from the scanned region. Indeed, it appears that the local composition of the  $\gamma'$  precipitate within 2 nm of the fault has been altered to account for the  $\eta$  phase formation. Recently, Makinen et al.<sup>19</sup> reported the presence of higher Al content just ahead of

the termination of SISFs inside a precipitate. That observation combined with Fig. 4(c) suggests all adjacent  $\gamma'$  phase to these faults are likely enriched in Al while depleted in the segregating elements, such as Co. The depletion of Co in Fig. 4(c) indicates that this region adjacent to the fault is the source of the Co that has segregated, rather than the  $\gamma$  phase being the source (where it is usually found in higher concentrations), via for example pipe diffusion along the partial dislocations. The proximity of these diffusion paths would reduce the time needed for these segregation events to occur. In fact, from the diffusion coefficients of Co ( $2.1 \times 10^{-19} \text{ m}^2 \text{ s}^{-1}$ ) and Al ( $3.9 \times 10^{-18} \text{ m}^2 \text{ s}^{-1}$ ) at 760 °C in ME3,<sup>33</sup> the time it would take for the diffusion observed in Fig. 4(c) to occur would be on the order of a few seconds. This is significantly faster than the estimated velocity ( $0.2 \text{ nm s}^{-1}$ )<sup>6,33</sup> of Cottrell atmospheres surrounding the leading dislocations ahead

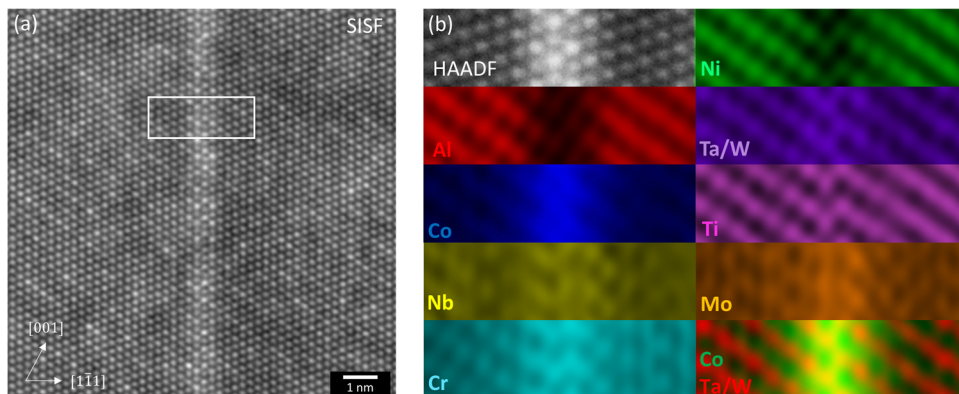


**Fig. 5 Atomic resolution characterization of a SISF in TSNA-1.** **a** HAADF STEM image of a SISF in TSNA-1 and **(b)** atomic resolution chemical maps of the SISF. The lowest right map is a composite of the Co and Ta/W maps revealing the  $\text{Co}_3(\text{W},\text{Ta})$   $\chi$  phase. Different colors were used to distinguish the different elements.

of the fault. Therefore, it can be concluded that the observed segregation occurs during fault formation and is not an evolutionary process underway at the fault lattice that occurred afterwards. Figure 5 reveals the composition and structure of a SISF in TSNA-1.

Turning attention now to the SISFs, the HAADF image in Fig. 5(a) reveals an ordered contrast along the fault similar to that observed in Co-based alloys, and has been interpreted as the formation of a local  $\text{D}0_{19}$   $\chi$  phase<sup>34</sup>. In Fig. 5(b), the first reported atomic-resolution chemical maps of a segregated SISF emphasizes that  $\chi$  phase has formed by Co segregating to Ni-sites along the SISF, while W (possibly Ta), Nb, Cr, and Mo have replaced Al at the Al-sites. Interestingly, no Ti content change was found between the SISF and adjacent  $\gamma'$  precipitate. These results confirm that the LPT strengthening involving both  $\eta$  and  $\chi$  phases are active during creep for the TSNA-1 alloy and contributing to its superior creep properties compared to other disk alloys. In Figs. 4 and 5, the Ta and W signals were combined and are indicated as Ta/W, due to the high error associated with deconvoluting their very close peaks. Though the high-resolution chemical maps in Fig. 4(b) and Fig. 5(b) provide great spatial clarity, they do not sufficiently reveal the subtle differences in the amount of segregation occurring between the two different faults. To better show the differences in elemental segregation between the SESF in Fig. 4(b) and SISF in Fig. 5(b), Supplementary Fig. 3 presents compositional line scans across both faults. From the line scans it's clear that both fault types show similar Ni and Al depletion and Co segregation. From Figs. 4(b) and 5(b) it's evident that the Co is replacing Ni on the Ni sub-lattice sites. The difference in the two phases is the propensity of other HCP formers segregating to the Al sublattice sites. The line scans in supplementary Fig. 3(c), 3(d) reveal a clear difference in the amount of Ti and Cr segregating to each fault type. In fact, Nb and Mo appear to also show slight differences in segregation tendency depending on the type of fault – where Nb segregates slightly more to the SESF and Mo more to the SISF. These observations reveal that local atomic structures along stacking faults will influence elemental segregation even in the same compositional environment.

**DFT evaluations.** TSNA-1 was produced to promote a Ta-rich  $\eta$  phase along SESFs and a W-rich  $\chi$  phase along SISFs. However, it has been revealed through other experiments that multiple alloying elements could possibly promote either phase. In fact, a recent study by Liljensten et al.<sup>22</sup> reported an Nb-rich  $\chi$  phase along SISFs which had not been considered a possible  $\chi$ -former previously. Therefore, to inform future alloy development

pursuits and explore the segregation differences between the SISF and SESF reported in this study, a phase stability study was performed exploring the influence that both major and minor alloying elements may have on  $\chi$  and  $\eta$  phase formations along with both fault types in Ni and Co-based alloys. DFT calculations of the three crystal structures presented in Supplementary Fig. 4 were fully relaxed for binary  $\text{Ni}_3\text{X}$  and  $\text{Co}_3\text{X}$  compositions where  $\text{X} = \text{Al}, \text{Ti}, \text{Zr}, \text{Hf}, \text{V}, \text{Nb}, \text{Ta}, \text{Cr}, \text{Mo}, \text{W}$ , and  $\text{Re}$ .

Especially for Ni-based superalloys, the terminal compositions of the  $\gamma'$  precipitate are  $\text{Ni}_3\text{Al}$  and  $\text{Ni}_3\text{X}$ , where element X differs from Al. Figure 6(a) shows the computed energy differences between the cubic  $\text{L}1_2$  ( $\gamma'$ ) and hexagonal structures  $\text{D}0_{19}$  ( $\chi$ ) or  $\text{D}0_{24}$  ( $\eta$ ) in  $\text{Ni}_3\text{X}$ , which depend on the composition and are altered if Al is (fully or partially) replaced by another element X.

With regards to Ni-based superalloys (Fig. 6(a)), Ta, Nb, and W appear to be the largest promoters of the  $\chi$  (blue) and  $\eta$  phase (black line) formation along SISFs and SESFs, respectively. However, for the  $\gamma$  formers Cr, Mo, W, and Re the formation energies (E) of  $\text{Ni}_3\text{X}$  compounds are either quite small or positive (unstable) and unlikely to form experimentally. Interestingly, from these DFT calculations, Ti does not appear to be a strong promoter of the  $\eta$  phase over  $\gamma'$ , especially when compared to Nb or Ta. Still, in a pure  $\text{Ni}_3\text{X}$  structure all the calculated elements appear to promote a phase transformation from  $\gamma'$  to  $\chi$  or  $\eta$  phase, except for Cr and Ti ( $\gamma' \rightarrow \chi$ ). With regards to Co-based superalloys, Fig. 6(b) indicates that Re, W, Mo, and Cr were found to be the best “major” element promoters of the hexagonal phases ( $\eta$  and  $\chi$ ) over cubic  $\gamma'$ . Overall, Nb, Ta, and W appear to be the most promising alloying elements to promote the formation of the strengthening  $\eta$  and  $\chi$  phases along the faults in Ni-base superalloys, especially since these elements are known  $\gamma'$  formers as well and would be able to segregate to  $\gamma'$  faults more quickly than  $\gamma$  formers due to their proximity to the defect. However, as Co superalloy content increases it would be expected that Mo, Re, and Cr could be promising additions as well. Importantly, Fig. 6 shows energy differences for the terminal compositions, while the dependence of energy versus composition is a non-linear continuous function. Nevertheless, any continuous function with particular values at the end points take all intermediate values between those endpoints. Hence, for any intermediate energy  $E_i$  between the terminal values there exist an intermediate composition  $x$ , at which  $E(x) = E_i$ . Importantly, this mathematical statement applied to energy differences helps to design precipitation-strengthened alloys. Figures 4 and 5 also reveal that Co segregates to both SISFs and SISFs by replacing Ni atoms on Ni-sites. This Co segregation was also explored using DFT calculations for both  $\text{L}1_2$ ,  $\text{D}0_{24}$ , and  $\text{D}0_{19}$  phases as shown in Fig. 7.

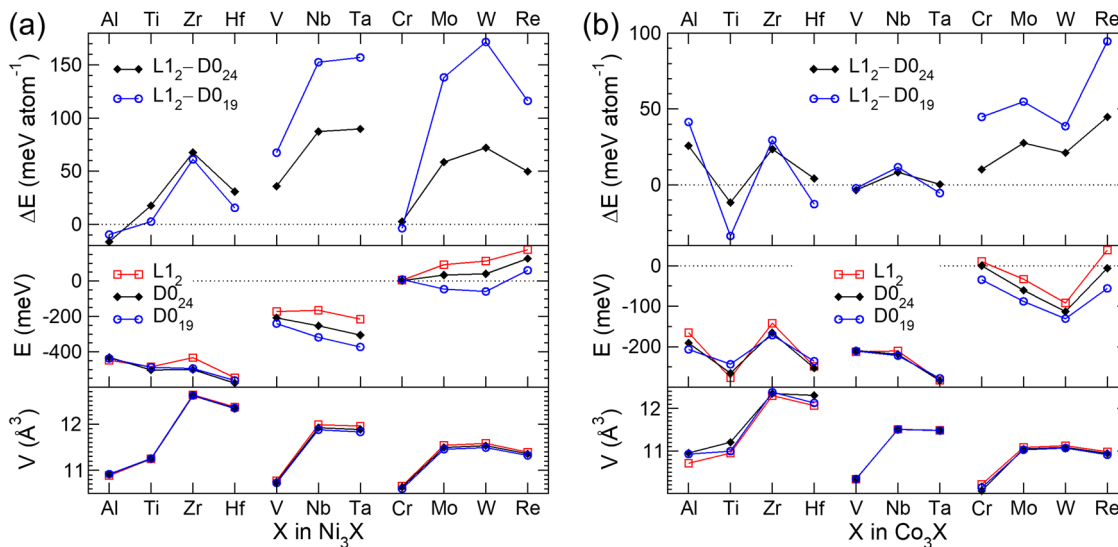


**Fig. 6 DFT calculation results.** Computed energy differences, formation energies (relative to the ground states of elemental solids), and volume per atom of L1<sub>2</sub> ( $\gamma'$ ), D0<sub>19</sub> ( $\chi$ ), and D0<sub>24</sub> ( $\eta$ ) structures, fully relaxed at zero pressure, for (a) binary Ni<sub>3</sub>X line compounds in nickel-based superalloys and (b) Co<sub>3</sub>X line compounds in cobalt-based superalloys with X = {Al, Ti, Zr, Hf, V, Nb, Ta, Cr, Mo, W, Re}. Elements are arranged by their group in the periodic table. Lines are only a guide to the eye.

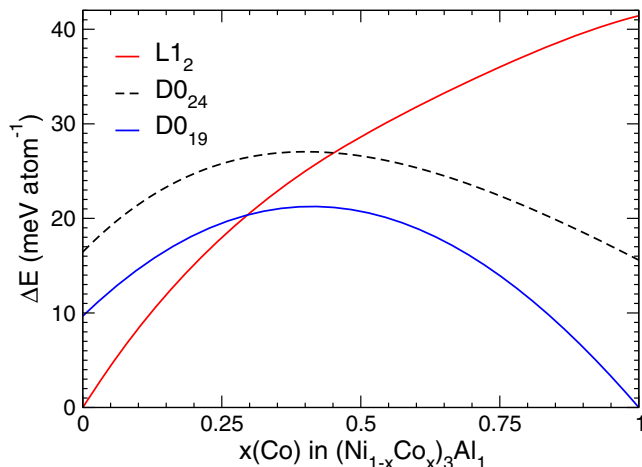


**Fig. 7 DFT predicts Co segregation on Ni sites along SSFs.** Mixing energy ( $\Delta E$ ) of (Ni<sub>1-x</sub>Co<sub>x</sub>)<sub>3</sub>Al<sub>1</sub> in L1<sub>2</sub> ( $\gamma'$ ), D0<sub>19</sub> ( $\chi$ ), and D0<sub>24</sub> ( $\eta$ ) structures are predicted by DFT to be concave versus composition; this points to Co segregation tendency along SSFs on Ni-sites. The computed VASP formation energies of Ni<sub>3</sub>Al (Co<sub>3</sub>Al) are -0.4477, -0.4381, and -0.4313 eV atom<sup>-1</sup> (-0.1652, -0.2066, and -0.1910 eV atom<sup>-1</sup>) in L1<sub>2</sub>, D0<sub>19</sub>, D0<sub>24</sub> phases, respectively.

The results in Fig. 7 reveal that segregation of Co would be expected on Ni-sites along SSFs as it would lower the energy of the fault which locally possesses a D0<sub>24</sub> or D0<sub>19</sub> crystal structure. The results are shown for a Ni<sub>3</sub>Al cell, though qualitatively similar segregation of Co is anticipated for Al mixed with other elements on the Al-sites. This may explain the presence of Co observed along SSFs in Ni-based superalloys post creep whether ordered phases ( $\eta$  and  $\chi$ ) or  $\gamma$ -like phase segregation was observed. Past work has revealed that Co is expected to lower stacking fault energy in these alloys and the results in Fig. 7 further confirm this<sup>35</sup>.

The research presented here combined with past studies<sup>22,36</sup> on phase transformations along SSFs provides a clearer picture of the compositional alloying space that might promote both  $\eta$  phase and  $\chi$  phase over  $\gamma$ -former segregation along faults in Ni-based

superalloys. For SESFs, the DFT results revealed that Ti does not appear to be as strong a promoter of  $\eta$  phase along SESFs as had been previously thought<sup>18</sup>. This has also been supported by experimental observation of  $\eta$  phase formation along SESFs in the Nb-rich RRHT5 but not in the Ti-rich LSHR even though each possessed similar Al/ $\eta$  phase former ratios (1.2 and 1.3, respectively)<sup>17,22</sup>. As such, the Al/ $\eta$  formers ratio may not be enough to predict  $\eta$  formation along SESFs. Instead, a weighted ratio containing both concentrations and the energy differences from Fig. 6 might be a better predictor. This predictor can be further improved by considering the non-linearity of energy differences versus composition. In addition, the lack of segregation of Ti along SISFs provides confirmation that these DFT calculations are accurate as Ti is the only experimentally evaluated element that was not calculated to promote the  $\chi$  phase for both Ni- and Co-rich systems. As additional alloys and their stacking fault segregation trends continue to be evaluated, combined with the calculations above, this alloy design space will become better defined along with improved methods to predict phase transformations along SSFs in Ni- and Co-based superalloys.

## Conclusion

In summary, a disk superalloy that promotes the recently discovered local  $\eta$  and  $\chi$  phase transformation strengthening mechanisms was successfully created and tested. TSNA-1 provided superior creep properties over the current state-of-the-art alloys ME3 and LSHR, and comparable creep strength as the blade alloy CMSX-4. The difference in creep properties between the four superalloys tested could not be explained by microstructural variations. Instead, the formation of  $\chi$  and  $\eta$  phases along the  $\gamma'$  stacking faults appears to correlate strongly with improved creep strength in TSNA-1. In addition, atomic resolution chemical maps and HAADF Z-contrast micrographs have revealed the specific lattice sites each segregating element was positioned along with each fault type and support the conclusion that ordered phases have nucleated along both SESFs and SISFs in TSNA-1. For future alloy development, an atomistic study found that Nb and Ta appear to be promising alloying elements for these new phase transformations along SISFs and SESFs, while

Re, W, and Mo appeared to be promising in alloys with significant Co concentrations. Therefore, researchers producing alloys with comparable amounts of Ni and Co should explore all five elements (Nb, Ta, Re, Mo, and W). Lastly, alloy designers should recognize that the atomic ratio of Al over  $\eta$  formers (Ti, Nb, Ta, plus Hf) may predict whether the strengthening  $\eta$  phase will form along SESFs during creep, though composition still needs to be considered. The more elaborate weighted ratio involving both concentrations and energy differences (from Fig. 6) is anticipated to be a more precise predictor. These combined conclusions reveal that future high-temperature Ni-base superalloys can be designed and optimized by controlling deformation at the atomic level.

## Methods

**Sample preparation.** For this study, a recently introduced disk alloy, Transformation Strengthened NASA Alloy 1 (TSNA-1)<sup>36</sup>, was produced and tested alongside three other Ni-base alloys with known segregation types along both faults (ME3, LSHR, and CMSX-4). Thus, these alloys provided a direct comparison between creep properties and the varying nature of LPT strengthening/softening along stacking faults. The compositions of these alloys are provided in Supplementary Table 3. ATI Powder Metals provided 25 kilograms of atomized and –270 mesh screened TSNA-1 powder. This alloy powder was then consolidated using a high temperature hot isostatic press (HIP) in stainless steel containers. The compact TSNA-1 alloy underwent a solution heat treatment at 1190 °C for 1 h followed by a conventional two-step aging at 855 °C for 4 h plus 775 °C for 8 h. Notably, the grain size of the heat-treated TSNA-1 alloy was found to be considerably finer compared to ME3 and LSHR, most likely a consequence of not forging or extruding the alloy before heat treatment. In contrast, the ME3 disk alloy was hot compacted, extruded, and isothermally forged into a flat pancake. Similarly, LSHR was also hot isostatically pressed, extruded, and isothermally forged into a flat pancake. ME3 and LSHR rectangular blanks were then machined and supersolvus solution heat-treated at 1171 °C for 1 h. Specimen of all three disk alloys were heat treated using the same equipment and air-cooled at the same average rate of approximately 72 °C per minute. ME3 underwent an aging heat-treated at 843 °C for 4 h plus 760 °C for 8 h while LSHR was heat-treated at 855 °C for 4 h plus 775 °C for 8 h. Additionally, a finer-grained LSHR alloy was also produced and tested in order to provide a better comparison to the TSNA-1 alloy.

**Mechanical testing.** Metcut Research Associates completed room temperature tensile tests for all three alloys in accordance to the ASTM E8 specification. Elevated temperature tensile tests at 760 °C were performed according to ASTM E21 specifications at NASA Glenn Research Center on both the fine grain LSHR and TSNA-1 alloys. These tests were interrupted at 1% strain to measure stress relaxation for 100 h. Metcut Research Associates also performed tensile creep tests at 760 °C and 552 MPa until about 0.3% plastic strain was reached. After the 0.3% plastic strain was reached the creep samples were cooled to room temperature under load in order to preserve the active deformation substructures.

**Microscopy.** Microstructural samples were prepared for SEM analysis using SiC grit paper to polish surfaces. After the 1200 grit polish step, each sample was further polished using a 0.5  $\mu\text{m}$  diamond suspension followed by a final refinement step using 0.05  $\mu\text{m}$  colloidal silica for 4 h in a vibratory polishing machine. SEM characterization of the  $\gamma'$  precipitates was performed on a Zeiss Auriga-FIB using an Everhart-Thornley secondary electron detector utilizing a 3 kV accelerating voltage. This low accelerating voltage minimizes contrast from sub-surface particles which would adversely impact the accuracy of the  $\gamma'$  analysis<sup>36</sup>. The grain structure and size of each alloy was examined using Electron Back-Scattered Diffraction (EBSD) using an EDAX Hikari EBSD detector with a 1  $\mu\text{m}$  spot size. TSL OIM Data Collection 7 software was used to process the EBSD orientation maps and provide average grain diameters where twin boundaries were excluded. Automated precipitate analysis was performed using NASA developed software written in Python 3. Segmentation was performed using the U-Net neural network architecture implemented in TensorFlow<sup>37</sup>. Precipitate sizes are given as equivalent spherical diameters. By using this machine learning approach on SEM micrographs that did not require an etching procedure to highlight precipitates, this characterization approach successfully removes user bias and error.

Post-mortem 3 mm diameter scanning transmission electron microscopy (STEM) disk samples were extracted from the gauge section of creep tensile specimens at a 45° angle from the stress axis using electrical discharge machining. The STEM samples were thinned to 130  $\mu\text{m}$  by hand using 600 grit SiC polishing paper. To achieve electron transparency the polished STEM disks were electro-polished using a solution of 90% methanol and 10% perchloric acid at –40 °C and 12 V using a Struers twin-jet polisher. Creep deformation analysis was performed on an FEI Talos at 200 kV using a high angle annular dark-field (HAADF) detector. Atomic resolution HAADF characterization of stacking faults was

achieved using a probe corrected FEI Themis at 200 kV. This atomic resolution HAADF imaging technique characterizes the presence of ordered structure along stacking faults by providing atomic number (Z) contrast information on atomic columns<sup>31,38</sup>. High-resolution EDS was performed using 4 Super-X detectors on the FEI Themis STEM using the FEI Velox software package. Cliff-Lorimer analysis<sup>39</sup> of the vertically integrated line scans were quantified using  $K_{\alpha}$  energies for Al, Ni, Co, Cr, Ti, Nb, and Mo, while  $L_{\alpha}$  energies were used for Ta and W. The Ta and W signals were combined in this study and are indicated as Ta/W, due to the high error associated with deconvoluting their very close peaks. The presented chemical maps are from lower resolution original spectral maps and averaged over a defined repeat unit based on the  $\eta$  and  $\chi$  phase crystal structure for improved resolution.

**DFT calculations.** The spin-polarized density functional theory was used to compute energies of the fully ordered and partially disordered periodic crystal structures<sup>25</sup>. The fully ordered structures were addressed using VASP code<sup>40,41</sup> with PAW-PBE pseudopotentials<sup>42,43</sup> and scripts from the TTK toolkit<sup>44</sup>. The structures with a homogeneous disorder on a sublattice were addressed using the coherent potential approximation<sup>45</sup> in the KKR-CPA code<sup>46</sup>. In both codes, the PBEsol<sup>47</sup> exchange-correlation functional was used. The Monkhorst-Pack<sup>48</sup>  $\Gamma$ -centered  $k$ -mesh with  $\geq 57$  points per  $\text{\AA}^{-1}$  was used for the Brillouin zone integration. Formation energies were computed relative to the energies of elemental solids in their ground states<sup>49</sup>.

## Data availability

The relevant datasets generated and analyzed throughout this work are available from the corresponding author upon reasonable request.

Received: 14 July 2021; Accepted: 23 September 2021;  
Published online: 14 October 2021

## References

1. Reed, R. *The Superalloys*. (Cambridge University Press, 2006).
2. Thornton, P. H., Davies, R. G. & Johnston, T. L. The temperature dependence of the flow stress of the gamma prime phase based upon Ni<sub>3</sub>Al. *Metall. Trans. A* **1**, 207–218 (1970).
3. Garosshen, T. J., Tillman, T. D. & McCarthy, G. P. Effects of B, C, and Zr on the structure and properties of a PM nickel base superalloy. *Metall. Trans. A* **18**, 69–77 (1987).
4. Jena, A. K. & Chaturvedi, M. C. Review of the role of alloying elements in the design of nickel-base superalloys. *J. Mater. Sci.* **19**, 3121–3139 (1984).
5. Vorontsov, V. A., Kovarik, L., Mills, M. J. & Rae, C. M. F. High-resolution electron microscopy of dislocation ribbons in a CMSX-4 superalloy single crystal. *Acta Mater.* **60**, 4866–4878 (2012).
6. Titus, M. S. et al. High resolution energy dispersive spectroscopy mapping of planar defects in L1<sub>2</sub>-containing Co-base superalloys. *Acta Mater.* **89**, 423–437 (2015).
7. Cantwell, P. R. et al. Grain boundary complexions. *Acta Mater.* **62**, 1–48 (2014).
8. Kuzmina, M., Herbig, M., Ponge, D., Sandlobes, S. & Raabe, D. Linear complexions: confined chemical and structural states at dislocations. *Science* **349**, 1080–1083 (2015).
9. Krause, A. R. et al. Review of grain boundary complexion engineering: know your boundaries. *J. Am. Ceram. Soc.* **102**, 778–800 (2018).
10. Song, H. Y., Zuo, X. D., An, M. R., Xiao, M. X. & Li, Y. L. Superplastic dual-phase nanostructure Mg alloy: a molecular dynamics study. *Comput. Mater. Sci.* **160**, 295–300 (2019).
11. Makineni, S. K. et al. Elemental segregation to antiphase boundaries in a crept CoNi-based single crystal superalloy. *Scr. Mater.* **157**, 62–66 (2018).
12. Viswanathan, G. et al. Segregation at stacking faults within the  $\gamma'$  phase of two Ni-base superalloys following intermediate temperature creep. *Scr. Mater.* **94**, 5–8 (2015).
13. Kontis, P. et al. The effect of chromium and cobalt segregation at dislocations on nickel-based superalloys. *Scr. Mater.* **145**, 76–80 (2018).
14. Barba, D., Smith, T. M., Miao, J., Mills, M. J. & Reed, R. C. Segregation-Assisted Plasticity in Ni-Based Superalloys. *Metall. Mater. Trans. A Phys. Metall. Mater. Sci.* **49**, 4173–4185 (2018).
15. Barba, D. et al. On the microtwinning mechanism in a single crystal superalloy. *Acta Mater.* **135**, 314–329 (2017).
16. Freund, L. P. et al. Segregation assisted microtwinning during creep of a polycrystalline L1<sub>2</sub>-hardened Co-base Superalloy. *Acta Mater.* **123**, 295–304 (2017).
17. Smith, T. M. et al. Effect of stacking fault segregation and local phase transformations on creep strength in Ni-base superalloys. *Acta Mater.* **172**, 55–65 (2019).

18. Smith, T. M. et al. Phase transformation strengthening of high temperature superalloys. *Nat. Commun.* **7**, 1–7 (2016).
19. Makineni, S. K. et al. On the diffusive phase transformation mechanism assisted by extended dislocations during creep of a single crystal CoNi-based superalloy. *Acta Mater.* **155**, 362–371 (2018).
20. Rae, C. M. F. & Reed, R. C. Primary creep in single crystal superalloys: origins, mechanisms and effects. *Acta Mater.* **55**, 1067–1081 (2007).
21. Rae, C. M. F., Matan, N. & Reed, R. C. The role of stacking fault shear in the primary creep of [001]-oriented single crystal superalloys at 750 °C and 750 MPa. *Mater. Sci. Eng.* **300**, 125–134 (2001).
22. Lilensten, L., Antonov, S., Gault, B., Tin, S. & Kontis, P. Enhanced creep performance in a polycrystalline superalloy driven by atomic-scale phase transformation along planar faults. *Acta Mater.* **202**, 232–242 (2021).
23. Zarkevich, N. A. Theoretical and computational methods for accelerated materials discovery. *Mod. Phys. Lett. B* **35**, 2130003 (2021).
24. Bouse, G. K. Eta and Platelet Phases in Investment Cast Superalloys. *Superalloys 1996 (Eighth Int. Symp.)* 163–172 (1996).
25. Maurer, G. E., Castledine, W., Schweizer, F. A. & Mancuso, S. Development of HIP Consolidated P/M Superalloys for Conventional Forging to Gas Turbine Engine Components. *Superalloys 1996* 645–652 [https://doi.org/10.7449/1996/superalloys\\_1996\\_645\\_652](https://doi.org/10.7449/1996/superalloys_1996_645_652) (1996).
26. Gabb, T. P. et al. The Effects of Heat Treatment and Microstructure Variations on Disk. *Superalloys 2008 (Eleventh Int. Symp.)* 121–130 (2008).
27. Ingesten, N. G., Warren, R. & Winberg, L. The Nature and Origin of Previous Particle Boundary Precipitates in P/M Superalloys. *High Temp. Alloy. Gas Turbines 1982* 1013–1027 (1982).
28. Kuo, Y. L. & Kakehi, K. Influence of powder surface contamination in the Ni-based superalloy 718 fabricated by selective laser melting and hot isostatic pressing. *Mater. (Basel.)* **7**, 3–13 (2017).
29. Kakehi, K. Effect of primary and secondary precipitates on creep strength of Ni-base superalloy single crystals. *Mater. Sci. Eng. A* **278**, 135–141 (2000).
30. Drew, G. L., Reed, R. C., Kakehi, K. & Rae, C. M. F. Single Crystal Superalloys: The Transition from Primary to Secondary Creep. *Superalloys 2004 (Tenth Int. Symp.)* 127–136 [https://doi.org/10.7449/2004/Superalloys\\_2004\\_127\\_136](https://doi.org/10.7449/2004/Superalloys_2004_127_136) (2004).
31. Pennycook, S. J. & Jesson, D. E. High-resolution Z-contrast imaging of crystals. *Ultramicroscopy* **37**, 14–38 (1991).
32. Pickering, E. J. et al. Grain-boundary precipitation in Allvac 718Plus. *Acta Mater.* **60**, 2757–2769 (2012).
33. Smith, T. M., Rao, Y., Wang, Y., Ghazisaeidi, M. & Mills, M. J. Diffusion processes during creep at intermediate temperatures in a Ni-based superalloy. *Acta Mater.* **141**, 261–272 (2017).
34. Titus, M. S. et al. Solute segregation and deviation from bulk thermodynamics at nanoscale crystalline defects. *Sci. Adv.* **2**, 1–8 (2016).
35. Yuan, Y. et al. Influence of Co content on stacking fault energy in Ni-Co base disk superalloys. *J. Mater. Res.* **26**, 2833–2837 (2011).
36. Smith, T. et al. Enhancing the creep strength of next-generation disk superalloys via local phase transformation strengthening. *Superalloys 2020 (Proceedings 14th Int. Symp. Superalloys)* 726–736 (2020).
37. Ronneberger, O., Fischer, P. & Brox, T. U-Net: Convolutional networks for biomedical image segmentation. *Int. Conf. Med. Image Comput. Comput. Interv.* 234–241 (2015).
38. Pennycook, S. J. Z-contrast transmission electron microscopy: direct atomic imaging of materials. *Annu. Rev. Mater. Sci.* **22**, 171–195 (1992).
39. Hoeft, H. & P. S. Investigations towards optimizing EDS analysis by the Cliff-Lorimer method in scanning transmission electron microscopy. *X-ray Spectrom.* **17**, 201–208 (1988).
40. Kresse, G. & Hafner, J. Ab initio molecular dynamics for liquid metals. *Phys. Rev. B* **47**, 558–561 (1993).
41. Kresse, G. & Hafner, J. Ab initio molecular-dynamics simulation of the liquid-metal-amorphous-semiconductor transition in germanium. *Phys. Rev. B* **49**, (1994).
42. Blochl, P. E. Projector augmented-wave method. *Phys. Rev. B* **50**, 17953–17979 (1994).
43. Kresse, G. & Joubert, D. From ultrasoft pseudopotentials to the projector augmented-wave method. *Phys. Rev. B* **59**, 1758–1775 (1999).
44. Zarkevich, N. A. & Johnson, D. D. Reliable first-principles alloy thermodynamics via truncated cluster expansion. *Phys. rev. Lett.* **92**, 255702 (2004).
45. Johnson, D. D., Nicholson, D. M., Pinski, F. J., Gyorffy, B. L. & Stocks, G. M. Density-Functional Theory for Random Alloys: Total Energy within the Coherent-Potential Approximation. *Phys. rev. Lett.* **56**, 2088–2091 (1986).
46. Johnson, D. D., Smirnov, A. V. & Khan, S. N. MECCA: Multiple-Scattering Electronic-Structure Calculations for Complex Alloys. (2015).
47. Perdew, J. P. et al. Restoring the Density-Gradient Expansion for Exchange in Solids and Surfaces. *Phys. rev. Lett.* **100**, 136406 (2008).
48. Monkhorst, H. J. & Pack, J. D. Special points for Brillouin-zone integrations. *Phys. Rev. B* **13**, 5188 (1976).
49. Zarkevich, N. A. Structural Database for Reducing Cost in Materials Design and Complexity of Multiscale Computations. *Complexity* **11**, 36–42 (2006).

## Acknowledgements

TMS, TPG, NAZ and JWJ acknowledge NASA's Aeronautics Research Mission Directorate (ARM) – Transformational Tools and Technologies Project and NASA's Advanced Air Transport Technology (AATT) Project Offices. AJE and MJM acknowledge the support of the National Science Foundation and the DMREF program under grant # 1922239. The high-resolution STEM imaging was performed at the Center for Electron Microscopy and Analysis (CEMAS) at OSU.

## Author contributions

TMS, TPG, and MJM designed and performed the experiments. TMS and AJE completed the microstructural characterization. TMS and JS executed and analyzed the machine learning  $\gamma'$  characterization. NAZ and JWJ performed the DFT modelling effort. TMS and TPG wrote the manuscript.

## Competing interests

The authors declare no competing interests.

## Additional information

**Supplementary information** The online version contains supplementary material available at <https://doi.org/10.1038/s43246-021-00210-6>.

**Correspondence** and requests for materials should be addressed to Timothy M. Smith.

**Peer review information** *Communications Materials* thanks the anonymous reviewers for their contribution to the peer review of this work. Primary Handling Editor: John Plummer. Peer reviewer reports are available.

**Reprints and permission information** is available at <http://www.nature.com/reprints>

**Publisher's note** Springer Nature remains neutral with regard to jurisdictional claims in published maps and institutional affiliations.



**Open Access** This article is licensed under a Creative Commons Attribution 4.0 International License, which permits use, sharing, adaptation, distribution and reproduction in any medium or format, as long as you give appropriate credit to the original author(s) and the source, provide a link to the Creative Commons license, and indicate if changes were made. The images or other third party material in this article are included in the article's Creative Commons license, unless indicated otherwise in a credit line to the material. If material is not included in the article's Creative Commons license and your intended use is not permitted by statutory regulation or exceeds the permitted use, you will need to obtain permission directly from the copyright holder. To view a copy of this license, visit <http://creativecommons.org/licenses/by/4.0/>.

This is a U.S. government work and not under copyright protection in the U.S.; foreign copyright protection may apply 2021